Multimode Optimization of the Phase-Shifted *LLC* Series Resonant Converter

Umme Mumtahina and Peter Joseph Wolfs, *Senior Member, IEEE*

***Abstract*—This paper presents a loss optimization method for phase-shifted *LLC* resonant converters operating with phase shift. The method features automatic detection of the preferred operational mode from the five possibilities for the topology. For a given power level and voltage transformation ratio it simultaneously determines the values of the resonant elements and transformer turns ratio. This work supplements and extends the available optimization tools for variable frequency operation and extends these to phase-shifted operation. The combined methods allow converters with much wider voltage regulation ranges to be designed. Numerical programming methods to determine the mode boundaries and to solve the steady-state solutions for the different modes of *LLC* converter are presented. A detailed loss model for a phase-shifted *LLC* is also discussed. A prototype of 30–403V, 295W is built to validate the optimization results. A comparison is made between an optimized and unoptimized converter. An extension to multipoint optimization, as required to optimize the European Weighted Efficiency is described.**

***Index Terms*—DC–DC power conversion, optimization methods, resonant power conversion.**

NOMENCLATURE

ω_o	Angular resonant frequency (LC).
ω_1	Angular resonant frequency ($(L+L_M)C$).
$V_{\rm base}$	Base voltage.
$\omega_{\rm base}$	Base angular frequency.
$Z_{\rm base}$	Base impedance.
$I_{\rm base}$	Base current.
$V_{\rm base}$	Base voltage.
$V_{\rm AB}$	Bridge voltage.
V_c	Capacitor voltage.
τ	Constraint set.
$P_{\rm cond\_pri}$	Conduction losses of primary MOSFETs.
C_{ds}	Drain source capacitance of primary MOSFETs.
V_f	Diode voltage drop.
η	Efficiency.
FF	Fill factor.
R_g	Gate resistance of primary MOSFETs.
$Q_{\rm gd}$	Gate-drain charge of primary MOSFETs.
$V_{\rm in}$	Input voltage.
V_1	Input voltage of *LLC* equivalent circuit.
I_L	Inductor current.
b_l	Lower bound vector.
I_M	Magnetizing current.
m_{M1}, m_{M2}	Mode indicators.
$V_{\rm gs,miller}$	Miller plateau voltage.
θ	Normalized angle.
θ_c	Normalized conduction angle.
γ	Normalized half-period.
F	Normalized switching frequency.
m_C	Normalized capacitor voltage.
j_L	Normalized inductor current.
m_M	Normalized magnetizing inductor voltage.
j_M	Normalized magnetizing inductor current.
j_o	Normalized average output current.
r_L	Normalized output load.
n_p	Number of primary turns.
n_s	Number of secondary turns.
$R_{\rm ds,on}$	On resistance of primary MOSFETs.
I_o	Output current.
V_o	Output voltage.
R_L	Output load.
P_o	Output power.
V_2	Output voltage of *LLC* equivalent circuit.
$I_{\rm rms-pri}$	Primary rms current.
l	Ratio of L and L_M.
k_1	Ratio of ω_1 and ω_o.
k_s	Ratio of $R_{\rm ac}$ and $R_{\rm dc}$.
f_o	Resonant frequency.
ρ	Resistivity of copper.
$P_{\rm cond,sec}$	Rectifier conduction loss.
f_s	Switching frequency.
k, α, β	Steinmetz coefficients.
x	Search variable vector.
n	Transformer turns ratio.
t	Time variable.
$T_{\rm off}$	Turn off time of primary MOSFETs.
$P_{\rm core}$	Transformer core loss.
$V_{\rm core}$	Transformer core volume.
ΔB	Transformer peak flux density.
$B_{\rm pk-pk}$	Transformer peak–peak flux density.
A_e	Transformer effective cross sectional area.
$P_{\rm winding}$	Transformer winding loss.
$R_{\rm ac}$	Transformer ac resistance.

Manuscript received August 24, 2017; revised December 12, 2017 and January 30, 2018; accepted January 31, 2018. Date of publication February 8, 2018; date of current version September 28, 2018. Recommended for publication by Associate Editor C. K. Tse. *(Corresponding author: Peter Joseph Wolfs.)*

U. Mumtahina is with the Engineering and Built Environment, Rockhampton, QLD 4701, Australia (e-mail: u.mumtahina@cqu.edu.au).

P. J. Wolfs is with the Central Queensland University, Faculty of Engineering and Physical Systems, North Rockhampton, QLD 4701, Australia (e-mail: p.wolfs@cqu.edu.au).

Color versions of one or more of the figures in this paper are available online at http://ieeexplore.ieee.org.

Digital Object Identifier 10.1109/TPEL.2018.2803741

R_{dc}	Transformer dc resistance.
MLT	Transformer Mean Length of Turn.
A_w	Transformer window area.
$P_{\mathrm{tot\_trans}}$	Total transformer loss.
P_{loss}	Total converter loss.
b_u	Upper bound vector.
L	Value of resonant inductor.
C	Value of resonant capacitor.
L_M	Value of magnetizing inductor.
M	Voltage conversion ratio.

I. Introduction

THE *LLC* resonant converter is a commercially popular topology that is an extension of the series resonant converter. A magnetizing inductor is added to overcome two problems found at light loads namely the loss of ZVS operation and the inability to regulate the light load voltage. For the conventional *LLC* the expressions for the voltage gain and the boundaries for ZVS operation are well known [1]–[4].

Generally the voltage is regulated in a *LLC* converter by the variable frequency control. This method can be analyzed using the following three basic approaches:

1) frequency domain analysis or first harmonic approximation (FHA) [5]–[8];
2) frequency domain analysis with time domain correction [9]–[11]; and
3) time domain analysis [12]–[15].

The application of the *LLC* converter over wide voltage and load ranges using predefined dead time control is presented in [6], [7], and [14]. A predefined normalized switching frequency range based on peak gain requirements is presented in [15]. Frequency control has been extensively studied for current limiting and protection. An over current protection method has been used to optimize *LLC* converter under short circuit condition in [9] by maximizing the resonant capacitor voltage. *LLC* converter has been used for battery charging application under short circuit condition [16]. Trajectory control has been used for optimizing *LLC* converter in [17], [18]. Other methods such as time weighted average efficiency, morphing control have been used for efficiency optimization [19], [20]. The above design methods try to find a single design solution but the inclusion of some arbitrary restrictions result in solutions that are not easily generalized. An alternative approach is to develop an algorithm, suitable for computer implementation, which can accurately calculate a solution where the user has discretion as to the preconditions and constraints that are applied.

Some new applications require *LLC* converters that can operate over a load range, which cannot be practically provided using just variable frequency control. For extreme load ranges very wide frequency ranges may be required forcing high losses at the higher frequencies and increasing the magnetic component sizing at the lower ranges. Phase-shifted control can be combined with variable frequency control [21]–[25] to extend the voltage regulation range. Phase shift control has also been used to suppress in-rush current [26], [27].

In an *LLC* with combined control modes the phase-shifted approach is used to reduce the voltage gain once the maximum operating frequency has been reached. This will be above resonance. An analytical model has been proposed to find the solution for state variables in discontinuous conduction mode in [28]. It is only applicable for specific modes and not all modes are considered. There is no closed form solution for the state variables at the transitions between switching states and that need to be found through an iterative numerical solution. Numerical calculation and programming tools have been used to solve steady-state equations of phase-shifted *LLC* converter in [29]. The results here are presented in graphical forms that allow modes to be determined on the basis of normalized converter variables.

The current published literature on optimizing the phase-shifted *LLC* converter is limited in comparison to the well-established variable frequency case. The variable duty cycle gives rise to a larger number of operational modes. In many applications, the converter specifications may be potentially satisfied by several competing designs that operate in different modes.

This paper is concerned with the optimization of the *LLC* converter in applications where a number of modes are possible. This situation becomes especially complex where one converter design must offer satisfactory performance at several loading conditions over a loading range.

Computer-aided optimization is an established concept for converter design and has been applied to a range of other converters [30]. All optimization tools include: a cost function that is used to numerically evaluate the performance of a proposed solution; a search method that proposes and evaluates a series of solution points; and a set of constraints upon the allowable range of solutions. A few examples of search methods include the following:

1) augmented Lagrangian penalty functions [30];
2) the Monte Carlo search methods [31];
3) intelligent search methods such as Genetic algorithms [32].

The major contribution of this paper is to develop a cost function that incorporates a multiple mode solver for the phase-shifted *LLC* state equations to provide a comprehensive solution. The multimode solver allows a cost function, based on the converter parameter set, to be evaluated. For a given set of converter parameters, the resultant operational mode of the phase-shifted *LLC* converter is identified and numerical solutions to the state variables are calculated. The mode solver can determine the current and voltage behavior of each mode. Once this information is at hand, a cost function can be evaluated and returned to the optimization engine.

In this paper, the multimode solution based cost function has been combined with the MATLAB optimization toolbox search method to minimize the losses, which is the main objective function for a particular solar energy application [33]. A loss model was developed to calculate the losses in the converter utilizing the state variable solutions obtained from the multimode solver. The optimization was used to maximize the efficiency of a module based 403Vdc output 295W dc–dc converter for distributed

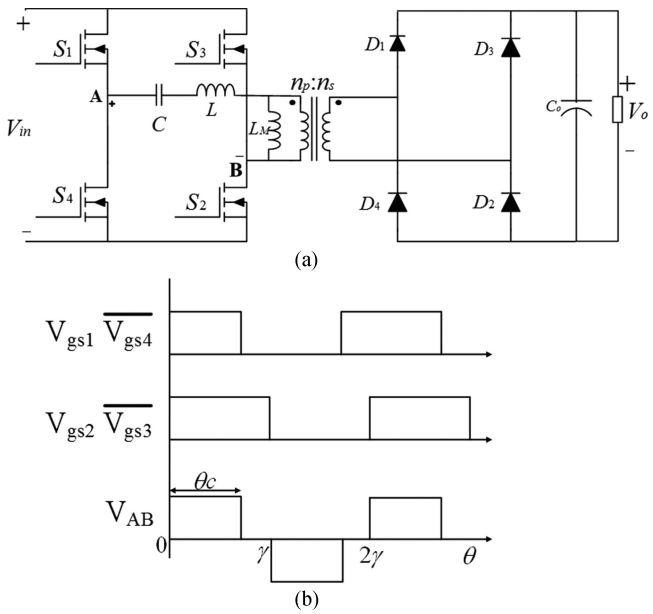

Fig. 1. (a) Full-bridge *LLC* resonant converter. (b) Phase-shifted gate signals between two switches.

maximum power point tracking (DMPPT) system. A prototype has been built to verify the optimization results. As in DMPPT system, the input voltage and output power will be varying at different times [34], [35], the European weighted efficiency is measured to show the effectiveness of this converter at different loads.

In principle, the multimode cost function can be readily combined with other optimization engines and configured to optimize other converter features.

II. Phase-Shifted *LLC* Mode Solver

LLC mode solver is central to the cost function evaluation for the optimization procedure. This solver contains all the steady-state equations of different modes and also the conditions to solve them numerically. There is a single continuous conduction mode in which the secondary rectifiers conduct throughout the cycle and discontinuous conduction modes in which the secondary diodes stop conducting at particular times. The input variables to this block are the input/output voltage, load, and the resonant parameters (L, L_M and C_r), etc. The output of this solver is the mode specific current and voltage waveforms. A detailed analysis of different modes in the mode solver has been discussed in following sections.

In full-bridge fixed-frequency phase-shifted *LLC* converter [Fig. 1(a)], switches are controlled by varying the duty cycle, which is shown in Fig. 1(b), where θ_c is the conduction angle. The following assumptions are considered for the analysis.

1) All passive components are ideal. The output capacitance of the primary switches and the junction capacitance of the rectifier diodes are ignored.
2) The output voltage is constant.
3) The dead time between the switches are ignored.

In order to simplify the analysis and results, the resonant characteristics of the tank are normalized. The normalized time variable θ is defined by

$$\theta = \omega_o t \tag{1}$$

where ω_o is the angular resonant frequency of the tank

$$\omega_o = \frac{1}{\sqrt{LC}} = 2\pi f_o. \tag{2}$$

A second resonant frequency appears when the secondary rectifiers are off which is denoted by ω_1:

$$\omega_1 = \frac{1}{\sqrt{(L + L_M)\, C}} \tag{3}$$

where L = resonant inductance, C = resonant capacitance, L_M = magnetizing inductance, and f_o = series resonant frequency. The ratio of two inductances is defined by

$$l = \frac{L}{L_M}. \tag{4}$$

The ratio of two resonant frequencies is defined by

$$k_1 = \frac{\omega_1}{\omega_o}. \tag{5}$$

A normalized half-period of switching cycle can be defined by

$$\gamma = \frac{\omega_o}{2f_s} = \frac{\pi}{F} \tag{6}$$

where f_s = switching frequency, F = normalized switching frequency. As the start of the half-period can be chosen arbitrarily, in this paper for simplicity the start of the half-period is chosen when the MOSFET S_2 is on at $\theta = 0$ and turns off at $\theta = \gamma$. This analysis is directed toward applications with a specified output voltage. Therefore, it is easier to define the base quantities with respect to the output. Base quantities are defined by

$$V_{\text{base}} = V_2 = \frac{n_p}{n_s} V_o = \frac{V_o}{n} \tag{7}$$

$$\omega_{\text{base}} = \omega_o \tag{8}$$

$$Z_{\text{base}} = \sqrt{L/C} \tag{9}$$

$$I_{\text{base}} = \frac{V_2}{Z_{\text{base}}} \tag{10}$$

$$M = \frac{V_2}{V_1} \tag{11}$$

where V_1 and V_2 are input and output voltages of *LLC* equivalent circuit, respectively, V_o is the output voltage, M is conversion ratio, n_p and n_s are number of transformer primary and secondary turns, and n is the transformer turns ratio, respectively. To denote normalized voltages and currents lowercase m and j are used, respectively, and the original variables are retained as subscripts:

$$m_X(\theta) = \frac{v_X(\theta/\omega_o)}{V_{\text{base}}} \tag{12}$$

$$j_Y(\theta) = \frac{i_Y(\theta/\omega_o)}{I_{\text{base}}}. \tag{13}$$

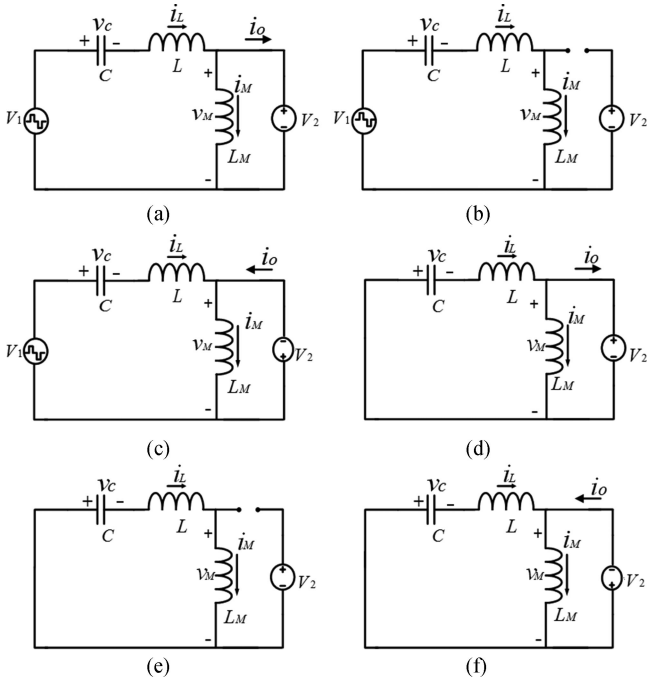

Fig. 2. Equivalent circuits of phase-shifted *LLC* converter.

The normalized output load resistance r_L is defined as

$$r_L = \frac{{n_p}^2 R_L}{{n_s}^2 Z_{\text{base}}}. \tag{14}$$

The operation of switching bridge is such that the terminal voltages are as shown in Fig. 1(b). In a full switching cycle, there are twelve equivalent circuit switching states. Due to odd symmetry only six of them are necessary to define the steady-state operation. The equivalent states are shown in Fig. 2.

A. Discontinuous Conduction Mode I (DCM I)

DCM I is the first mode considered. This mode comprises three equivalent circuits Fig. 2(a), (d), and (e). The time domain current and voltage waveforms and steady-state trajectory of DCM I are shown in Fig. 3. The steady-state equations of DCMI are given below.

For $(0 \le \theta \le \theta_1)$

$$m_C(\theta) = (m_C(0) - 1/M + 1)\cos(\theta) + j_L(0)\sin(\theta) + 1/M - 1 \tag{15a}$$

$$j_L(\theta) = \left(-m_C(0) + \frac{1}{M} - 1\right)\sin(\theta) + j_L(0)\cos(\theta) \tag{15b}$$

$$m_M(\theta) = 1 \tag{15c}$$

$$j_M(\theta) = j_M(0) + l(\theta) \tag{15d}$$

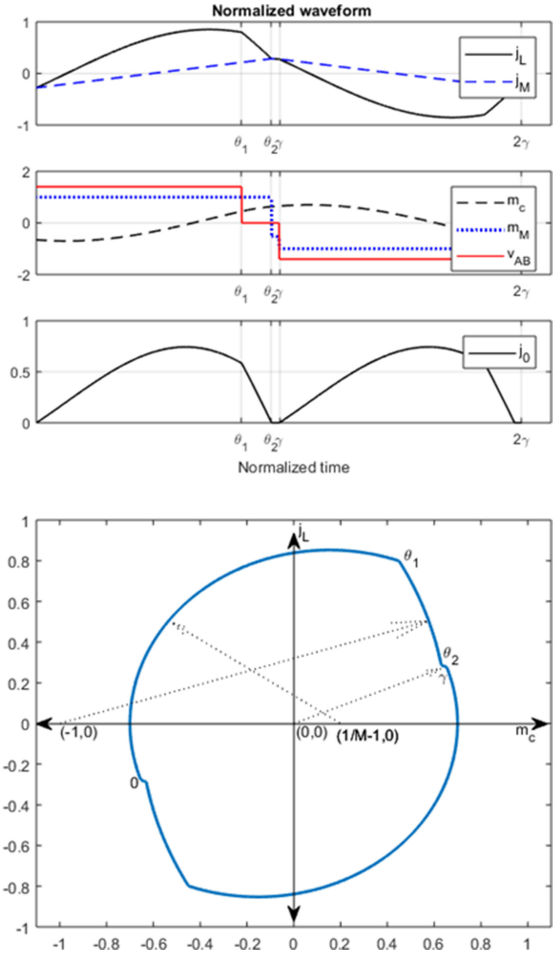

Fig. 3. Ideal time domain waveforms and steady-state trajectory of DCM I.

For $(\theta_1 \le \theta \le \theta_2)$

$$m_C(\theta) = (m_C(\theta_1) + 1)\cos(\theta_2 - \theta_1) + j_L(\theta_1)\sin(\theta_2 - \theta_1) - 1 \tag{16a}$$

$$j_L(\theta) = -(m_C(\theta_1) + 1)\sin(\theta_2 - \theta_1) + j_L(\theta_1)\cos(\theta_2 - \theta_1) \tag{16b}$$

$$m_M(\theta) = 1 \tag{16c}$$

$$j_M(\theta) = j_M(\theta_1) + l(\theta_2 - \theta_1). \tag{16d}$$

For $(\theta_2 \le \theta \le \gamma)$

$$m_C(\theta) = \left({}^1/_{k_1}\right) j_L(\theta_2)\sin[k_1(\gamma - \theta_2)] + m_C(\theta_2)\cos[k_1(\gamma - \theta_2)] \tag{17a}$$

$$j_L(\theta) = j_L(\theta_2)\cos[k_1(\gamma - \theta_2)] - k_1 m_C(\theta_2)\sin[k_1(\gamma - \theta_2)] \tag{17b}$$

$$m_M(\theta) = \frac{\{-m_C(\theta_2)\cos[k_1(\gamma - \theta_2)] - \left({}^1/_{k_1}\right) j_L(\theta_2)\sin[k_1(\gamma - \theta_2)]\}}{(1 + l)} \tag{17c}$$

$$j_L(\theta) = j_M(\theta). \tag{17d}$$

In these equations, there are five unknowns $m_C(0), j_L(0), \theta_1$, θ_2, and M. These unknowns can be solved by the following equations, which are the base of the solver:

$$m_C(0) + m_C(\gamma) = 0 \tag{18a}$$

$$j_L(0) + j_L(\gamma) = 0 \tag{18b}$$

$$j_L(\theta_1) - j_M(\theta_1) = 0 \tag{18c}$$

$$j_M(0) + j_M(\gamma) = 0 \tag{18d}$$

$$j_o r_L = 1 \tag{18e}$$

where j_o is the average output current and is expressed as

$$\begin{aligned} j_o &= \frac{1}{\gamma}\int_0^{\gamma} |j_L(\theta) - j_M(\theta)| d\theta \\ &= \frac{1}{\gamma}\int_0^{\theta_1} |j_L(\theta) - j_M(\theta)| d\theta \\ &\quad + \frac{1}{\gamma}\int_{\theta_1}^{\theta_3} |j_L(\theta) - j_M(\theta)| d\theta \\ &= \frac{1}{\gamma}[\{1/M - 1 - m_C(0)\}\{1 - \cos(\theta_1)\} \\ &\quad + j_L(0)\sin(\theta_1) - j_L(0)\theta_1 - \frac{1}{2} l {\theta_1}^2 \\ &\quad + j_L(\theta_1)\sin(\theta_2 - \theta_1) \\ &\quad + (m_C(\theta_1) + 1)\cos(\theta_2 - \theta_1) \\ &\quad - j_M(\theta_1)(\theta_2 - \theta_1) \\ &\quad - \frac{1}{2} l (\theta_2 - \theta_1)^2]. \end{aligned} \tag{19}$$

MATLAB function *fsolve* (*x*), which is a numerical-based search function has been used to find a numerical solution to the unknowns. During an optimization process, the values found can be used to verify the operating mode using the method shown in Fig. 4. After finding the unknowns, the mode distribution equations are applied to check whether the converter is operating in DCM I or not. The voltage across the magnetizing inductance determines in which mode the converter is operating. Two mode indicators ($m_{M1}(\theta)$ and $m_{M2}(\theta)$) defined as the normalized voltage on L_M determine whether the diodes start to conduct or not. According to Kirchhoff's voltage law from Fig. 2(b)

$$m_L(\theta) + m_C(\theta) + m_{M1}(\theta) = \frac{1}{M}.$$

$m_{M1}(\theta)$ can be rewritten as

$$m_{M1}(\theta) = \frac{-m_C(\theta) + 1/M}{1 + l}. \tag{20}$$

Similarly, $m_{M2}(\theta)$ can be written from Fig. 2(e) as

$$m_{M2}(\theta) = \frac{-m_C(\theta)}{1 + l}. \tag{21}$$

For simplicity, two conditions such as $\theta = 0$ and $\theta = \gamma$ would be considered. If $|m_{M1}(0) \geq 1|$, then the secondary diode conducts and assumption of DCM I mode is true. Otherwise, If $|m_{M1}(0) < 1|$, the secondary diode is off and assumption of DCM I mode is not true and it might be another mode. If $|m_{M2}(\gamma) \leq 1|$, then assumption of DCM I mode is true.

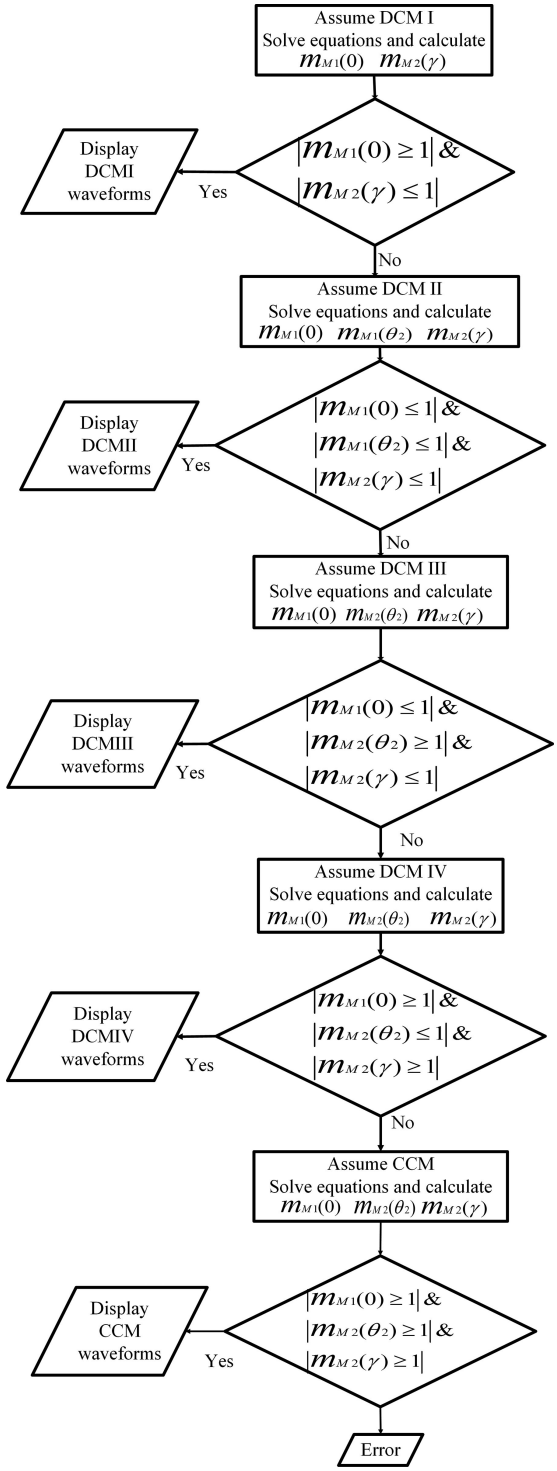

Fig. 4. Flowchart to distinguish different modes.

B. Discontinuous Conduction Mode II (DCM II)

The converter can operate in DCM II mode. The equivalent circuits for this mode are shown in Fig. 2(a), (b), and (e).

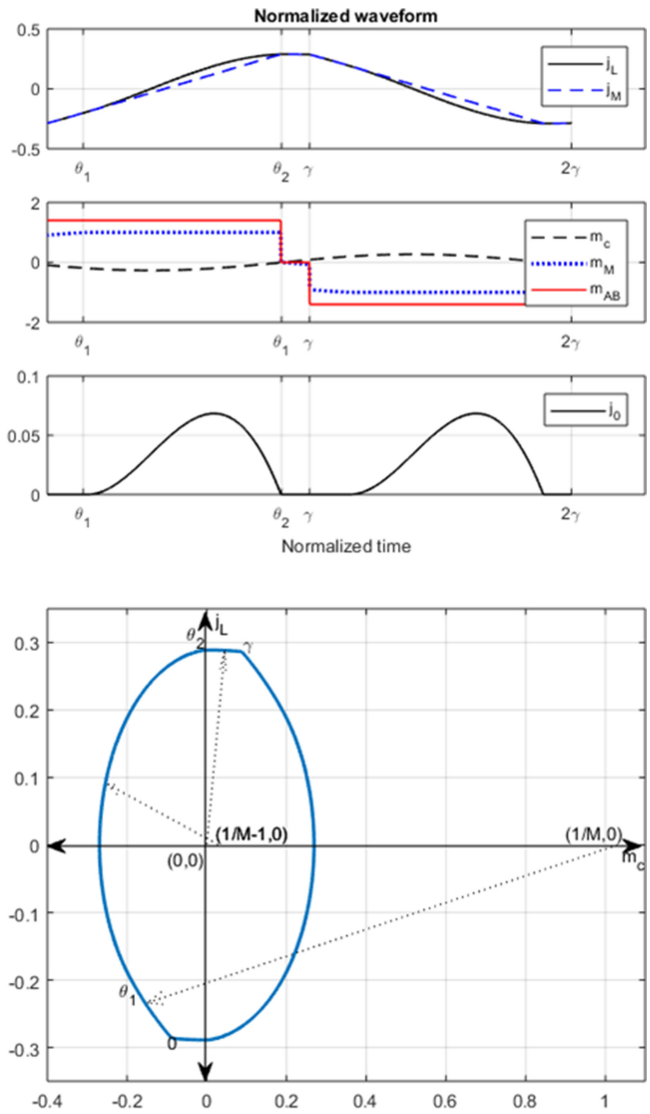

Fig. 5. Ideal time domain waveforms and steady-state trajectory of DCM II.

The current and voltage waveforms and steady-state trajectory of DCM II are shown in Fig. 5. There are five unknowns $m_C(0)$, $j_L(0)$, θ_1, θ_2, and M, which can be solved by these following equations:

$$m_C(0) + m_C(\gamma) = 0 \tag{22a}$$
$$j_L(0) + j_L(\gamma) = 0 \tag{22b}$$
$$j_L(\theta_1) - j_M(\theta_1) = 0 \tag{22c}$$
$$j_L(\theta_2) - j_M(\theta_2) = 0 \tag{22d}$$
$$j_o r_L = 1. \tag{22e}$$

After finding the unknowns, the same procedures have been carried out for DCM II as that for DCM I. If $|m_{M1}(0) \leq 1|$, $|m_{M1}(\theta_2) \leq 1|$, and $|m_{M2}(\gamma) \leq 1|$, then the assumption of DCM II is true.

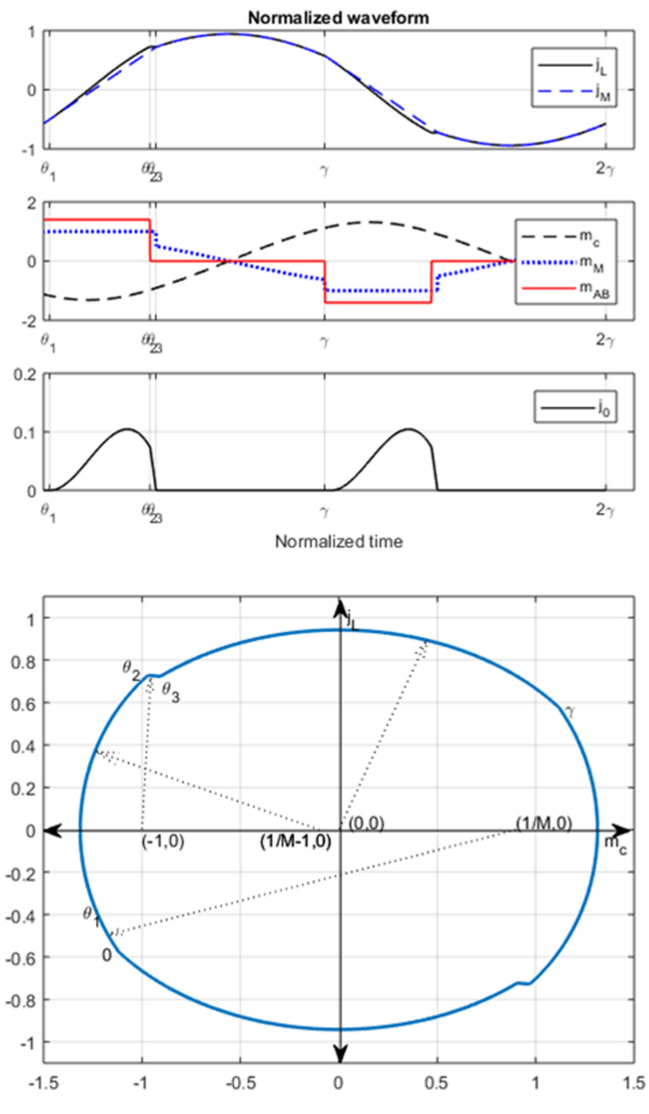

Fig. 6. Ideal time domain waveforms and steady-state trajectory of DCM III.

C. Discontinuous Conduction Mode III (DCM III)

The converter can also operate in DCM III mode. The equivalent circuits for this mode are shown in Fig. 2(a), (b), (d), and (e). The current and voltage waveforms and steady-state trajectory of DCM III are shown in Fig. 6. There are six unknowns $(m_C(0), j_L(0), \theta_1, \theta_2, \theta_3, M)$, which can be solved by these following equations:

$$m_C(0) + m_C(\gamma) = 0 \tag{23a}$$
$$j_L(0) + j_L(\gamma) = 0 \tag{23b}$$
$$j_M(0) + j_M(\gamma) = 0 \tag{23c}$$
$$j_L(\theta_1) - j_M(\theta_1) = 0 \tag{23d}$$
$$j_L(\theta_3) - j_M(\theta_3) = 0 \tag{23e}$$
$$j_o r_L = 1. \tag{23f}$$

After finding the unknowns, the same procedures have been carried out for DCM III as that for DCM I. If $|m_{M1}(0) \leq 1|$,

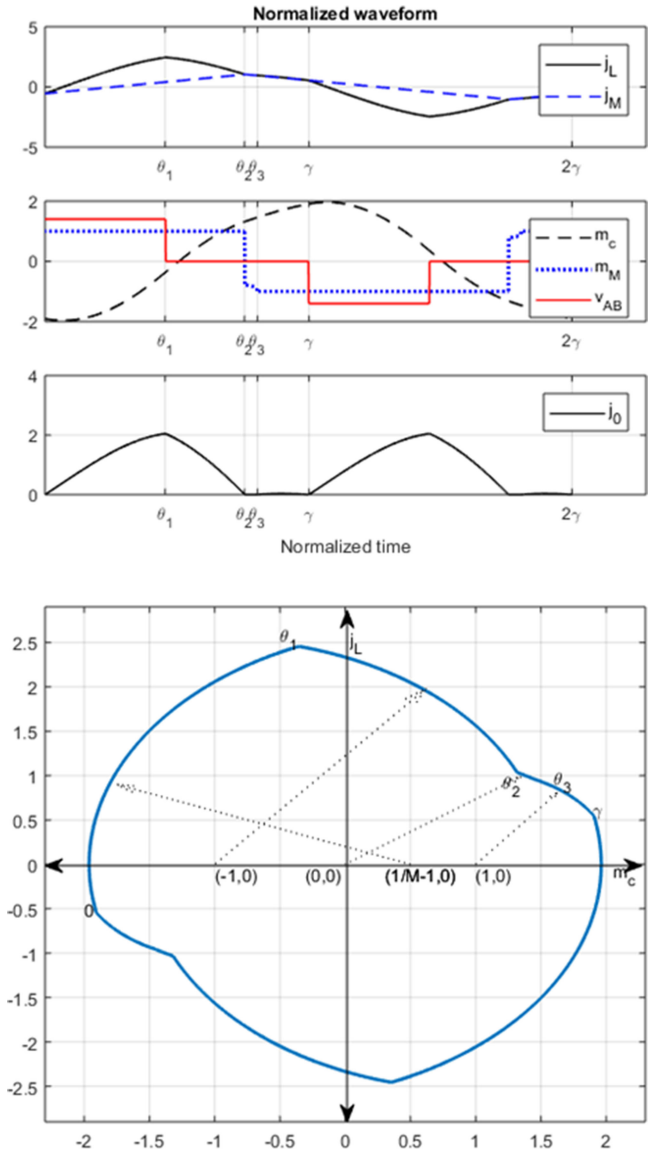

Fig. 7. Ideal time domain waveforms and steady-state trajectory of DCM IV.

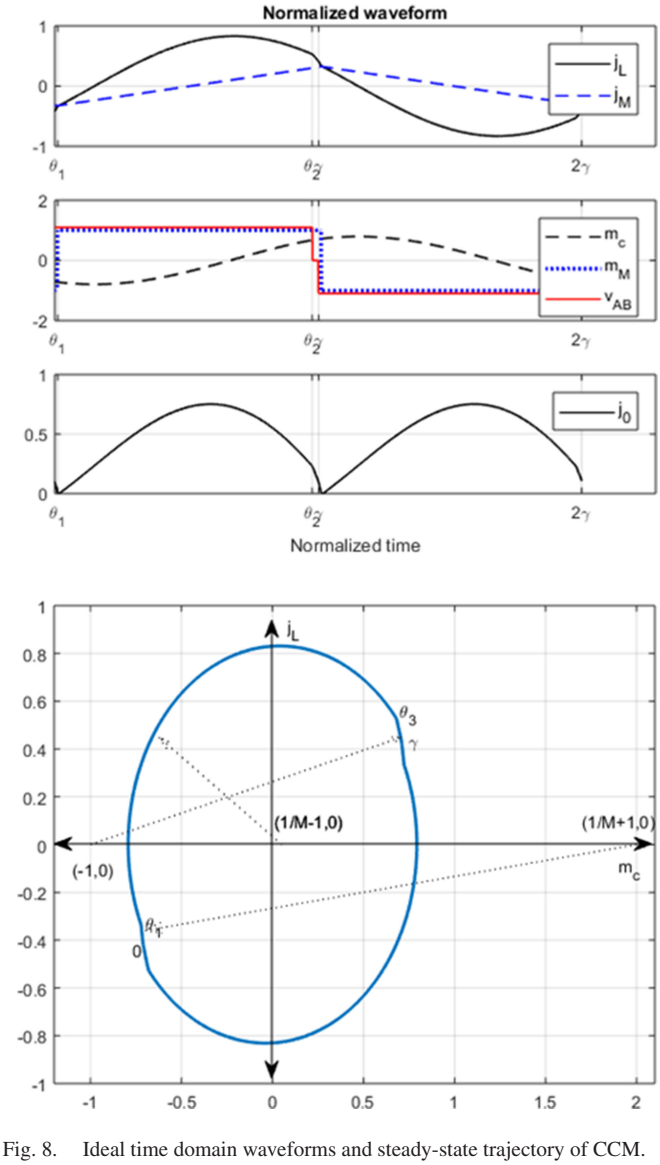

Fig. 8. Ideal time domain waveforms and steady-state trajectory of CCM.

$|m_{M2}(\theta_2) \geq 1|$, and $|m_{M2}(\gamma) \leq 1|$, then the assumption of DCM III is true.

D. Discontinuous Conduction Mode IV (DCM III)

There is another operation mode which is called discontinuous conduction mode IV (DCM III). The current and voltage waveforms and steady-state trajectory of DCM III are shown in Fig. 7. Though this mode is not used in practice due to the failure of its soft switching condition, it is included in the solver to complete the solver operation.

E. Continuous Conduction Mode (CCM)

The CCM mode exists when the load is relatively high and the conduction angle is large. The conversion ratio for this mode is less than unity. The equivalent circuits for this mode are shown in Fig. 2(a), (c), and (d). The current and voltage waveforms and steady-state trajectory of CCM are shown in Fig. 8. In this mode, there are five unknowns ($m_C(0)$, $j_L(0)$, θ_1, θ_2, M) which can be solved by these following equations:

$$m_C(0) + m_C(\gamma) = 0 \tag{24a}$$

$$j_L(0) + j_L(\gamma) = 0 \tag{24b}$$

$$j_M(0) + j_M(\gamma) = 0 \tag{24c}$$

$$j_L(\theta_1) - j_M(\theta_1) = 0 \tag{24d}$$

$$j_o r_L = 1. \tag{24e}$$

This mode is also validated by the similar procedure. If $|m_{M1}(0) \geq 1|$, $|m_{M2}(\theta_2) \geq 1|$, and $|m_{M2}(\gamma) \geq 1|$, then the assumption of CCM I is true.

III. Loss Calculation

A. Mosfet Losses

In the mode solver, the operation mode determines the current waveforms and to predict the conduction losses, the current

harmonics and RMS current are calculated by the fast Fourier transform. The conduction losses of the primary MOSFETs are denoted by

$$P_{\text{cond\_pri}} = 4{I_{\text{rms-pri}}}^2 R_{\text{ds,on}} \tag{25}$$

where $R_{ds,\text{on}}$ is the on resistance of the primary MOSFET.

In these optimization procedures, it is considered that the switches accomplish ZVS condition so that turn on losses and diode recovery losses of MOSFETs are neglected. However, there is a crossover of current and voltage during the turn off transition, which can be calculated from [36]. The total turn off losses can be expressed as

$$P_{\text{off}} = \frac{2}{3} V_{\text{in}} \left[\frac{n V_o \theta_c}{4 L_M \gamma f_s} - C_{\text{ds}} \frac{V_{\text{in}}}{T_{\text{off}}} \right] T_{\text{off}} f_s \tag{26}$$

where C_{ds} is the drain source capacitance of the main switches and T_{off} is the turn off time and can be calculated by

$$T_{\text{off}} = \frac{R_g Q_{\text{gd}}}{V_{\text{gs,miller}}} \tag{27}$$

where R_g is the gate resistance, Q_{gd} is the gate-drain charge, and $V_{\text{gs,miller}}$ is the Miller plateau voltage.

B. Transformer Losses

Transformer core loss can be calculated by the original Steinmetz equation [37]

$$P_{\text{core}} = k f_s^{\alpha} \Delta B^{\beta} V_{\text{core}} \tag{28}$$

where $k, \alpha,$ and β are the Steinmetz coefficients derived from the manufacturer datasheet, V_{core} is the core volume, and ΔB is the peak flux density and it can be calculated by

$$\Delta B = \frac{1}{2} B_{\text{pk-pk}} = \frac{1}{2} \frac{\int_0^{\frac{1}{f_s}} |v_M(t)|\, dt}{n_p A_e} \tag{29}$$

where $B_{\text{pk-pk}}$ is the peak–peak flux density, v_M is voltage across the magnetizing inductance, and A_e is the effective cross-sectional area of the transformer. Transformer winding losses can be calculated as

$$P_{\text{winding}} = {I_{\text{rms-pri}}}^2 R_{\text{ac}} \tag{30}$$

where R_{ac} is the ac resistance of the transformer and can be calculated from this equation:

$$R_{\text{ac}} = k_s R_{\text{dc}} \tag{31}$$

The ratio (k_s) of the ac to dc resistance (R_{dc}) is a function of the construction quality of transformer. It is considered to be constant during the optimization. In this paper, it is assumed that high-quality materials are available and k_s is set to be one. R_{dc} can be calculated by

$$R_{\text{dc}} = \frac{\rho \times \text{MLT} \times n^2}{\text{FF} \times A_w} \tag{32}$$

where ρ is the resistivity of copper, MLT is mean length of turn, FF is the fill factor, and A_w is the window area. Total transformer losses will be

$$P_{\text{tot\_trans}} = P_{\text{core}} + P_{\text{winding}}. \tag{33}$$

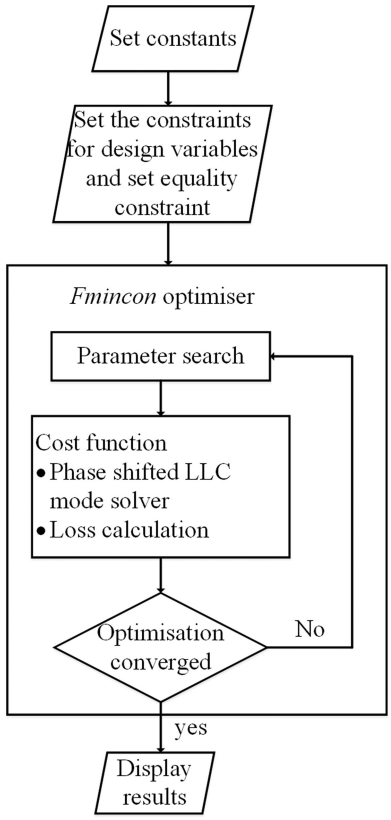

Fig. 9. Flowchart of optimization procedure.

C. Rectifier Losses

The output rectifiers will have the soft switching condition so that they will have only conduction losses which can be expressed as

$$P_{\text{cond,sec}} = \frac{2 P_o}{V_0} V_f \tag{34}$$

where P_o is converter output power and V_f is the on drop voltage of each diode.

IV. Optimization Procedure

To begin the optimization, the constant parameters are first set. These include discrete component parameters such as device resistances, diode drops, the input and output voltage, and the output power. Fig. 9 shows the total optimization procedure. The design variables for this optimization procedure are n_p, n_s, L_M, C, and L and all these variables are denoted by one search variable vector x:

$$x = [n_p, n_s, L_M, C, L]. \tag{35}$$

A constraint set τ is set for these search variables which is expressed as

$$\tau = \{b_l \le x \le b_u\} \tag{36}$$

where b_l is lower-bound vector and b_u is the upper-bound vector. Voltage regulation is considered as an equality constraint that is

TABLE I
OPTIMIZED DESIGN VARIABLES

Design variables	Lower boundary	Upper boundary	Optimized variables
n_p	3	9	6 (integer)
n_s	70	90	80
$L_M\,(\mu\mathrm{H})$	8	20	15
$C(\mu\mathrm{F})$	0.5	5	0.88
$L(\mu\mathrm{H})$	1	10	2.4

TABLE II
LOSS DISTRIBUTION OF THE COMPONENTS

Components	Loss (W)
Primary MOSFET conduction	1.5
Primary MOSFET switching	0.15
Rectifier	1.68
Transformer core	0.87
Transformer winding loss	1.4
Total losses (calculated)	5.6
Efficiency	98.1%

expressed as

$$\frac{V_o}{V_{\text{in}}} = \frac{n_s M}{n_p}. \tag{37}$$

Voltage gain M has a nonlinear relation with design variables. As part of the optimization process, the converter mode will be determined for each set of search variables so that the voltage constrain is maintained. The cost function of this optimization is to minimize the losses at full load, which is denoted by $P_{\text{loss}}(x)$. The cost function block includes (Fig. 9) the mode solver equations and also the loss calculation.

The MATLAB optimization function *fmincon* (*x*) is used as an optimization search engine because it is fast and robust. "Active set algorithm" has been used within this search engine for the optimization. The solution times are typically in the range of 2 min. It is recognized that *fmincon* returns a continuous value for the turns ratio. In this paper, the turns are rounded to integer values. It is possible to utilize the existing mode selector and cost functions with a range other optimization approaches that will explicitly consider the turn numbers as integer variables. This will be at the expense of computational speed.

V. RESULTS

A. Optimized Results

This paper aims to optimize a phase-shifted *LLC* converter with input/output voltage 30 V/403 V and with a 295 W or 550 Ω load. The switching frequency is 115 kHz. Table I summarizes the optimized design variables in which the lower-bound and upper-bound parameters are given. Physical factors limit these boundaries. For primary turns integer value is considered but the closest turns ratio is maintained. Calculated loss distribution from the optimized program is also presented in Table II. In the optimization procedure, losses in the control system are not considered. The optimized efficiency is calculated by

$$\eta = \frac{P_o}{P_o + P_{\text{loss}}}. \tag{38}$$

After the optimization, the converter falls into CCM mode which is shown in Fig. 10.

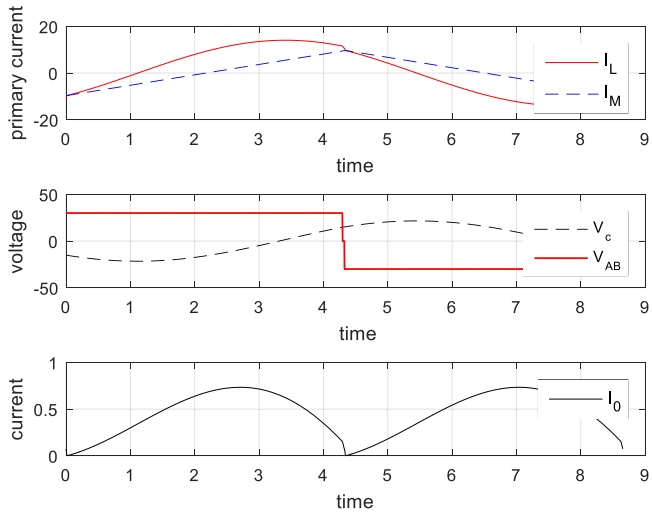

Fig. 10. Current and voltage waveforms at optimized efficiency (30 V, full load).

TABLE III
UNOPTIMIZED DESIGN VARIABLES

Design variables	Unoptimized variables
n_p	6
n_s	80
$L_M\,(\mu\mathrm{H})$	11
$C(\mu\mathrm{F})$	1.3
$L(\mu\mathrm{H})$	2.4

B. Unoptimized Results

A traditional design approach, as described in [38]–[40], has been applied to choose the design variables for an unoptimized condition. The design variables are summarized in Table III.

C. Experimental Results

Two prototypes of the converter have been built for experimental verification and the optimized converter is shown in Fig. 11. The two versions of the converter, using the component values in Tables I and III, allow comparisons between and optimized and unoptimized case. The semiconductor part numbers and the component values for the optimized converter are given in Table IV. The measured efficiency of the optimized prototype at 30 V, full load is 97.9%. The European weighted efficiency of the converter at 30 V, full load is 96.4%. The full load waveforms are shown in Fig. 12. In this paper, every experimental figure has three traces (red = resonant inductor current (I_L), purple = resonant capacitor voltage (V_c), green

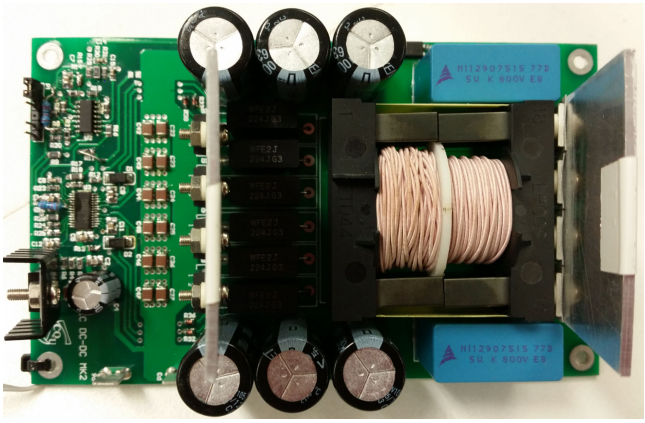

Fig. 11. Prototype of phase-shifted *LLC* converter.

TABLE IV
PARAMETERS FOR EXPERIMENTAL PROTOTYPE

Parameter	Value
MOSFETs	IPP 027N08N5
Rectifiers	STTH 20R04
Transformer	ETD 44/22/15 N87
	Turns ratio 6:80
	Litz wire (0.04 mm × 180 strands)
	Core gap 0.478 mm
	Leakage inductance 2.4 μH
	Magnetizing inductance 14.99 μH
Resonant capacitor	0.88 μF Metalized polypropylene
Output capacitor	10 μF

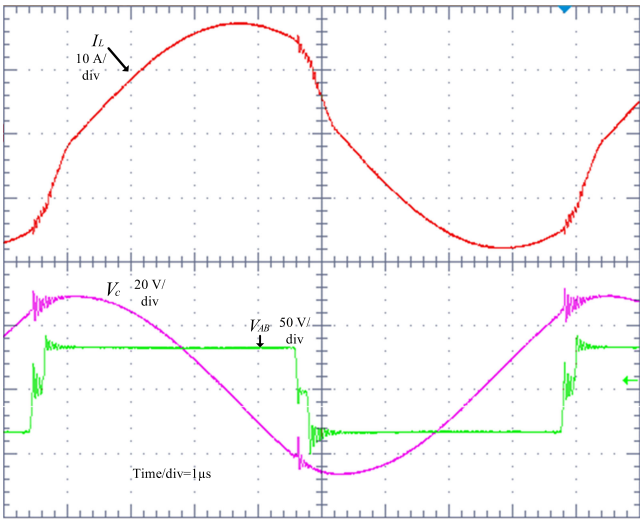

Fig. 12. Current and voltage waveforms of optimized converter at 30 V, full load.

= bridge voltage (V_{AB})). The experimental and analytical results are in close agreement. Some variation is expected due to the need to select rational turns ratio. In Fig. 12, there are high frequency disturbances in capacitor voltage at the bridge switching edges. This is a measurement artifact due to the oscilloscope CMRR.

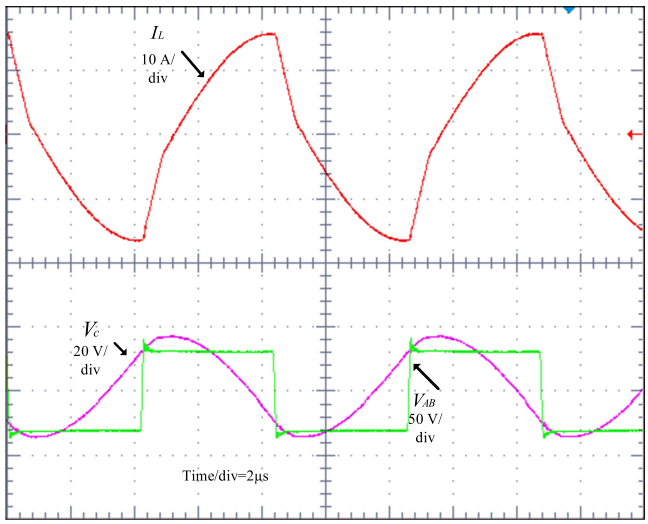

Fig. 13. Current and voltage waveforms of un-optimized converter at 30 V, full load.

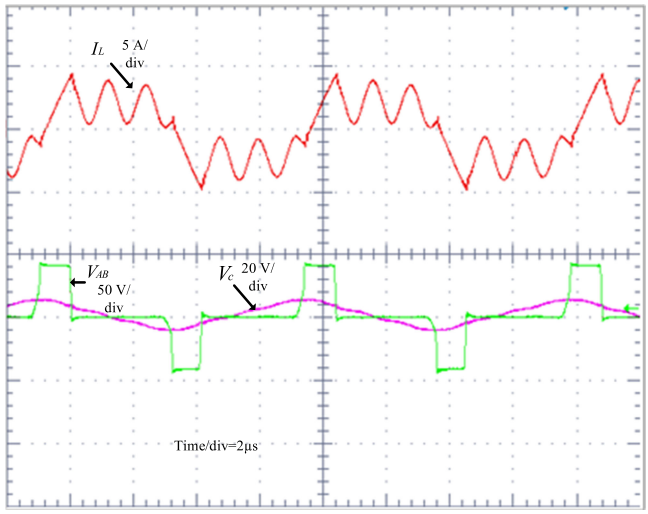

Fig. 14. Current and voltage waveforms of optimized converter at 40 V, 5% load.

A feature of the optimization process is that it has been identified as continuous mode and driven the duty cycle to close to 100%, which certainly minimizes the conduction loss component within the overall cost function. The experimental waveforms for the unoptimized converter is shown in Fig. 13. The key difference between these two is that the unoptimized converter has a higher magnetizing current that increases the conduction losses. For any converter, once the converter parameters are fixed during the design phase, operations at part load will require a reduction in the duty cycle to maintain the voltage regulation.

This paper examines the two worst case conditions, which are shown in Fig. 14 (maximum output voltage, minimum power) and Fig. 15 (minimum input voltage, maximum power). When the converter operates at maximum input voltage and minimum load, the ringing appears due to the secondary rectifier and leakage inductance. The optimization process, upon which the hardware design is based, selected the continuous mode on the

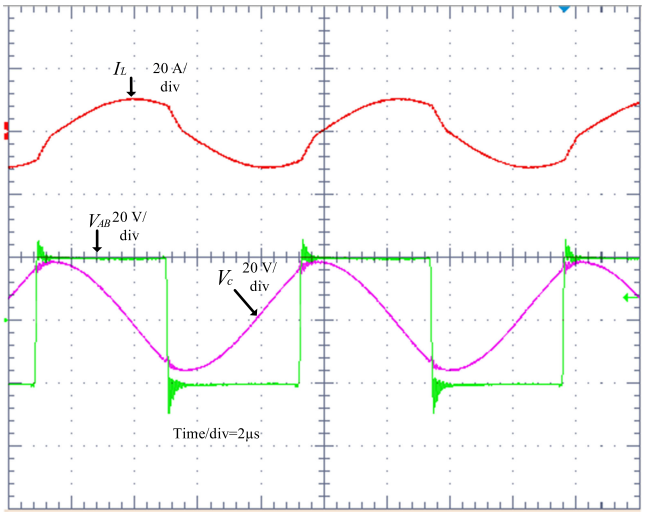

Fig. 15. Current and voltage waveforms of optimized converter at 20 V, full load.

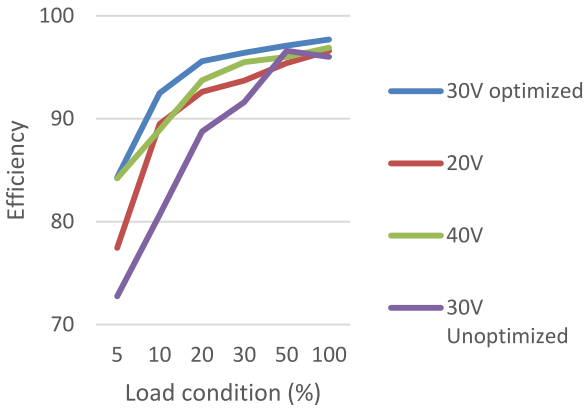

Fig. 16. Efficiency measurement at different load conditions for different voltage levels.

basis of superior losses. The experimental converter runs in the continuous mode is all cases other than extreme light load cases. One DCM mode emerges at light load. That DCM mode is shown in Fig. 14. There are other DCM modes but these will not occur in this experimental equipment because of the component values produced by the optimization method. The other modes will exist in other converters with suitable physical component values. The efficiency curves of the unoptimized and optimized converter are plotted in Fig. 16. The optimized converter shows better results at nominal voltage for all load conditions.

VI. Conclusion

This paper has presented a multimode optimization method for the phase-shifted *LLC* resonant converter. The method allows a designer to specify the required power level along the input and output voltages. For a given set of power electronic devices, the multimode optimizer will then select the key resonant components, the transformer turns ratio, the bridge phase shift and the operating mode that result in the minimum losses.

All optimization systems include a cost function, a search method, and a set of constraints. The key contribution of this paper is the development of a cost function that includes a mode solver and a loss estimation function. The mode selection must satisfy the inherent constraints imposed by the operational power and voltage gain specification. The mode solver consists of state equations of all the modes and a method to determine the associated initial conditions for each switching state. For a particular specifications for fixed input/output voltage and load, the operational mode is identified and numerical solution to the state variables are calculated. The solver determines the current and voltage waveforms. A loss model has been developed to calculate the losses based on the information found from the solver. In combination, the mode solver and loss calculation function form a cost function calculator which can then be embedded in an optimization system.

In this paper, a MATLAB optimization search engine is applied. The *fmincon* routine is used as an optimization engine because it is fast and robust. The multimode solver can be readily combined with other optimization search engines including many popular intelligent methods such as Genetic Algorithms (GA) or Particle Swarm Optimization (PSO).

The optimized results are well matched with experimental results. In this paper an optimization was presented for a single operating point which is full load at nominal voltage. As the transformer turns ratio was a free variable in the optimization process the solution converged upon the continuous conduction mode. This is expected as the continuous modes are favorable with respect to conduction losses.

It is straight forward to extend the cost function for the simultaneous weighted optimization of converters at several loads as would be required for the optimization of the European weighted efficiency. For each load condition, a cost needs to be evaluated and these are combined with weightings to give an overall cost. In this case the optimization becomes more interesting as the requirement to share just one transformation ratio amongst several loading conditions will force the adoption of different modes. It is likely the continuous mode will be adopted at high load conditions and discontinuous modes will be selected at partial loadings.

References

[1] M. Jabbari, H. Kazemi, N. Hematian, and G. Shahgholian, "A novel resonant *LLC* soft-switching buck converter," in *Proc. IEEE 23rd Int. Symp. Ind. Electron.*, 2014, pp. 370–374.

[2] H. N. Vu, D. D. Tran, and C. Woojin, "A novel hybrid soft switching full-bridge PWM and full-bridge *LLC* converter for on-board battery charger applications," in *Proc. IEEE 8th Int. Power Electron. Motion Control Conf.*, 2016, pp. 2470–2473.

[3] M. Pajnić, P. Pejović, Z. Despotović, M. Lazić, and M. Skender, "Design consideration for high frequency *LLC* resonant converter with matrix transformer," in *Proc. Int. Symp. Power Electron.*, 2017, pp. 1–6.

[4] N. Shafiei, M. A. Saket, and M. Ordonez, "Time domain analysis of *LLC* resonant converters in the boost mode for battery charger applications," in *Proc. IEEE Energy Convers. Congr. Expo.*, 2017, pp. 4157–4162.

[5] S. D. Simone, C. Adragna, C. Spini, and G. Gattavari, "Design-oriented steady-state analysis of *LLC* resonant converters based on FHA," in *Proc. Int. Symp. Power Electron. Electr. Drives, Autom. Motion*, 2006, pp. 200–207.

[6] L. Bing, L. Wenduo, L. Yan, F. C. Lee, and J. D. van Wyk, "Optimal design methodology for *LLC* resonant converter," in *Proc. IEEE Appl. Power Electron. Conf.*, 2006, pp. 1–6.

[7] R. Beiranvand, B. Rashidian, M. R. Zolghadri, and S. M. H. Alavi, "Optimizing the normalised dead-time and maximum switching frequency of a wide-adjustable-range *LLC* resonant converter," *IEEE Trans. Power Electron.*, vol. 26, no. 2, pp. 462–472, Feb. 2011.

[8] R. Beiranvand, B. Rashidian, M. R. Zolghadri, and S. M. H. Alavi, "A design procedure for optimizing the *LLC* resonant converter as a wide output range voltage source," *IEEE Trans. Power Electron.*, vol. 27, no. 8, pp. 3749–3763, Aug. 2012.

[9] X. Xie, J. Zhang, C. Zhao, Z. Zhao, and Z. Qian, "Analysis and optimization of *LLC* resonant converter with a novel over-current protection circuit," *IEEE Trans. Power Electron.*, vol. 22, no. 2, pp. 435–443, Mar. 2007.

[10] C. Oeder, A. Bucher, J. Stahl, and T. Duerbaum, "A comparison of different design methods for the multiresonant *LLC* converter with capacitive output filter," in *Proc. IEEE Control Model. Power Electron.*, 2010, pp. 1–7.

[11] G. Ivensky, S. Bronshtein, and A. Abramovitz, "Approximate analysis of resonant *LLC* DC–DC converter," *IEEE Trans. Power Electron.*, vol. 26, no. 11, pp. 3274–3284, Apr. 2011.

[12] J. F. Lazar and R. Martinelli, "Steady-state analysis of the *LLC* series resonant converter," in *Proc. IEEE Appl. Power Electron. Conf.*, 2001, vol. 2, pp. 728–735

[13] T. Liu, Z. Zhou, A. Xiong, J. Zeng, and J. Ying, "A novel precise design method for *LLC* series resonant converter," in *Proc. 28th Int. Telecommun. Energy Conf.*, 2006, pp. 1–6.

[14] C. Adragna, S. D. Simone, and C. Spini, "A design methodology for *LLC* resonant converters based on inspection of resonant tank currents," in *Proc. IEEE Appl. Power Electron. Conf.*, 2008, pp. 1361–1367.

[15] X. Fang *et al.*, "Efficiency-oriented optimal design of the *LLC* resonant converter based on peak gain placement," *IEEE Trans. Power Electron.*, vol. 28, no. 5, pp. 2285–2296, May 2013.

[16] F. Musavi, M. Craciun, D. S. Gautam, W. Eberle, and W. G. Dunford, "An *LLC* resonant DC-DC converter for wide output voltage range battery charging applications," *IEEE Trans. Power Electron.*, vol. 28, no. 12, pp. 5437–5445, Dec. 2013.

[17] W. Feng, F. C. Lee, and P. Mattavelli, "Simplified optimal trajectory control (SOTC) for *LLC* resonant converters," *IEEE Trans. Power Electron.*, vol. 28, no. 5, pp. 2415–2426, May 2013.

[18] R. Zheng, B. Liu, and S. Duan, "Analysis and parameter optimization of start-up process for *LLC* resonant converter," *IEEE Trans. Power Electron.*, vol. 30, no. 12, pp. 7113–7122, Dec. 2015.

[19] Z. Fang, T. Cai, S. Duan, and C. Chen, "Optimal design methodology for *LLC* resonant converter in battery charging applications based on time-weighted average efficiency," *IEEE Trans. Power Electron.*, vol. 30, no. 10, pp. 5469–5483, Oct. 2015.

[20] M. M. Jovanović and B. T. Irving, "On-the-fly topology-morphing control and efficiency optimization method for *LLC* resonant converters operating in wide input- and/or output-voltage range," *IEEE Trans. Power Electron.*, vol. 31, no. 3, pp. 2596–2608, Mar. 2016.

[21] B. McDonald and F. Wang, "*LLC* performance enhancements with frequency and phase shift modulation control," in *Proc. IEEE Appl. Power Electron. Conf.*, 2014, pp. 2036–2040.

[22] M. Yu, D. Sha, and X. Liao, "Hybrid phase shifted full bridge and *LLC* half bridge DC–DC converter for low-voltage and high-current output applications," *IET Power Electron.*, vol. 7, no. 7, pp. 1832–1840, Jul. 2014.

[23] J. H. Kim, C. E. Kim, J. K. Kim, J. B. Lee, and G. W. Moon, "Analysis on load-adaptive phase-shift control for high efficiency full-bridge *LLC* resonant converter under light-load conditions," *IEEE Trans. Power Electron.*, vol. 31, no. 7, pp. 4942–4955, Jul. 2016.

[24] S. M. S. I. Shakib and S. Mekhilef, "A frequency adaptive phase shift modulation control based *LLC* series resonant converter for wide input voltage applications," *IEEE Trans. Power Electron.*, vol. 32, no. 11, pp. 8360–8370, Nov. 2017.

[25] W. Xuan, W. Guangzhu, W. Yubin, S. Xiaowei, and O. Zhujian, "Three-level half-bridge *LLC* converter with phase shift and frequency modulation control," in *Proc. IEEE Ind. Electron. Soc.*, 2016, pp. 1429–1434.

[26] D. Yang, C. Chen, S. Duan, J. Cai, and L. Xiao, "A variable duty cycle Soft startup strategy for *LLC* series resonant converter based on optimal current-limiting curve," *IEEE Trans. Power Electron.*, vol. 31, no. 11, pp. 7996–8006, Nov. 2016.

[27] S. Liu, R. Ren, W. Meng, X. Zheng, F. Zhang, and L. Xiao, "Short-circuit current control strategy for full-bridge *LLC* converter," in *Proc. IEEE Energy Convers. Congr. Expo.*, 2014, pp. 3496–3503.

[28] Y. Shen, H. Wang, F. Blaabjerg, X. Sun, and X. Li, "Analytical model for *LLC* resonant converter with variable duty-cycle control," in *Proc. IEEE Energy Convers. Congr. Expo.*, 2016, pp. 1–7.

[29] W. Liu, B. Wang, W. Yao, Z. Lu, and X. Xu, "Steady-state analysis of the phase shift modulated *LLC* resonant converter," in *Proc. IEEE Energy Convers. Congr. Expo.*, 2016, pp. 1–5.

[30] S. Balachandran and F. C. Y. Lee, "Algorithms for power converter design optimization," *IEEE Trans. Aerosp. Electron. Syst.*, vol. AES-17, no. 3, pp. 422–432, May 1981.

[31] N. D. Benavides and P. L. Chapman, "Mass-optimal design methodology for DC–DC converters in low-power portable fuel cell applications," *IEEE Trans. Power Electron.*, vol. 23, no. 3, pp. 1545–1555, May 2008.

[32] C. Choon-Keat and S. R. R. Kondapalli, "Modeling, analysis, simulation and design optimization (Genetic Algorithm) of DC-DC converter for uninterruptible power supply applications," in *Proc. Int. Conf. Power Electron. Drives Syst.*, 2005, pp. 1530–1535.

[33] T. LaBella, W. S. Yu, J. S. Lai, M. Senesky, and D. Anderson, "A bidirectional-switch-based wide-input range high-efficiency isolated resonant converter for photovoltaic applications," *IEEE Trans. Power Electron.*, vol. 29, no. 7, pp. 3473–3484, Jul. 2014.

[34] M. A. G. d. Brito, L. Galotto, L. P. Sampaio, G. de Azevedo e Melo, and C. A. Canesin, "Evaluation of the main MPPT techniques for photovoltaic applications," *IEEE Trans. Ind. Electron.*, vol. 60, no. 3, pp. 1156–1167, Mar. 2013.

[35] S. B. Kjaer, J. K. Pedersen, and F. Blaabjerg, "A review of single-phase grid-connected inverters for photovoltaic modules," *IEEE Trans. Ind. Appl.*, vol. 41, no. 5, pp. 1292–1306, Sep.–Oct. 2005.

[36] J. H. Kim, C. E. Kim, J. K. Kim, and G. W. Moon, "Analysis for *LLC* resonant converter considering parasitic components at very light load condition," in *Proc. IEEE Energy Convers. Congr. Expo. Asia*, 2011, pp. 1863–1868.

[37] C. P. Steinmetz, "On the law of hysteresis," *Trans. Am. Inst. Electr. Eng.*, vol. 9, no. 1, pp. 1–64, Jan. 1892.

[38] S. Tian, F. C. Lee, and Q. Li, "Equivalent circuit modeling of *LLC* resonant converter," in *Proc. IEEE Appl. Power Electron. Conf.*, 2016, pp. 1608–1615.

[39] G. Rubino, L. Rubino, N. Serbia, P. Ladoux, and P. Marino, "*LLC* resonant converters in PV applications comparison of topologies considering the transformer design," in *Proc. Int. Conf. Clean Electr. Power*, 2013, pp. 37–41.

[40] C. H. Chang, C. A. Cheng, and H. L. Cheng, "Modeling and design of the *LLC* resonant converter used as a solar-array simulator," *IEEE J. Emerg. Sel. Top. Power Electron.*, vol. 2, no. 4, pp. 833–841, Dec. 2014.

Umme Mumtahina received the B.S. degree in electrical and electronics engineering from Chittagong University of Engineering and Technology, Chittagong, Bangladesh, in 2012. She is currently working toward the Ph.D. degree in power electronics from the Central Queensland University, Rockhampton, Queensland, Australia.

She is also working as a Research Assistant with the Central Queensland University. Her research interests include renewable energy conversion, dc–dc power converters, and switch mode power converters.

Peter Joseph Wolfs (M'79–SM'97) is with the School of Engineering and Technology, Central Queensland University, Rockhampton, Queensland, Australia. His research interests include power electronics applications for solar energy, smart grid technology, distributed renewable resources, and energy storage impacts on system capacity and power quality.

Prof. Wolfs is a Fellow of Engineers Australia and a Registered Professional Engineer in the State of Queensland.